AKARI/FIS All-Sky Survey Bright Source Catalogue Version 1.0 Release Note

I. Yamamura, S. Makiuti, N. Ikeda, Y. Fukuda, S. Oyabu, T. Koga (ISAS/JAXA),
G. J. White (RAL/OU)

Version 1.0, March 30, 2010

Abstract

The AKARI/FIS Bright Source Catalogue Version 1.0 provides the positions and fluxes of 427,071 point sources in the four far-infrared wavelengths centred at 65, 90, 140, and 160 μm. The sensitivity in the 90 μm band is about 0.55 Jy.

This document describes the data format and definitions of contents, and the characteristics of the release catalogue. The outline of the data processing and calibration are also explained. The users of the catalogue are requested to carefully read this document, especially Sections 4, 5, and 7 before using the data in quantitative scientific discussions.

Any questions and comments are appreciated via ISAS Helpdesk *iris_help@ir.isas.jaxa.jp*.

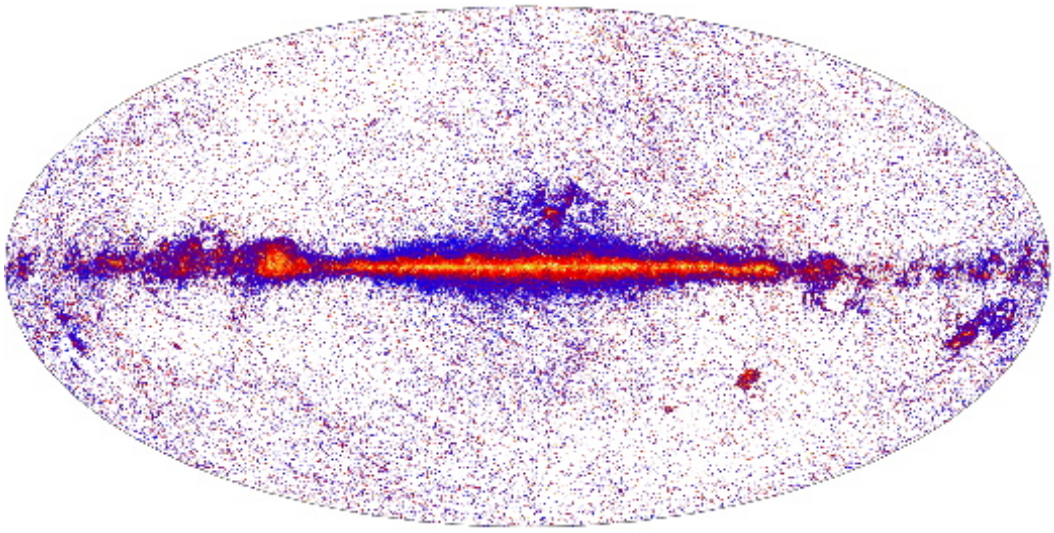

The far-infrared source detected by AKARI/FIS at 90 μm.

Update history		
2010/03/30		Document Version 1 release.

Contents

1 Overview

1.1 The AKARI All-Sky Survey

The Infrared Astronomical Satellite AKARI (Murakami et al. 2007) was launched on February 21th, 2006 (UT). After three weeks in performance verification phase (PV) (April 13th to May 7th), Phase 1 observations started on the May 8th and continued until November 9th, followed by Phase 2 observations until exhaustion of the liquid Helium on the August 26th, 2007. One of the main objectives of the AKARI mission was to carry out an all-sky survey in four photometric bands in the far-infrared spectral region centred at 65, 90, 140, and 160 μm with the Far-Infrared Surveyor instrument (FIS; Kawada et al. 2007), and in two mid-infrared bands centred at 9 and 18 μm with the Infrared Camera (IRC; Onaka et al. 2007). The All-Sky Survey had the highest priority during Phase 1 operations. In Phase 2 the observation plan was highly optimized to fill the scan gaps caused in Phase 1 under constraints of carrying out the maximum number of pointed observations. As the result the FIS scanned 98 percent of the entire sky more than twice during the 16 months of the cryogenic mission phase. The AKARI/FIS Bright Source Catalogue is the primary data product from the AKARI survey. The catalogue is supposed to have a uniform detection limit (corresponding to per scan sensitivity) over the entire sky (except for high background regions where we had to apply different data acquisition mode). Redundant observations are used to increase the reliability of the detection.[1] Two β version catalogues, β-1 and 2, have been made available to the AKARI science team members for initial scientific analysis and assessment. The first public version of the catalogue includes many improvements that are based on the comments from the users on the team, and their accumulated experiences of the AKARI data reduction and processing.

In the following text this catalogue is also referred to as the "FIS catalogue".

[1]The AKARI/FIS Faint Source Catalogue, in which the data redundancy is used to improve the detection limit, is a future project.

1.2 The Far-Infrared Surveyor (FIS)

The specifications of the FIS instrument are summarized in Table 1. It provides four photometric bands between 50 and 180 μm, with two broad bands and two narrow bands. Individual detector systems were implemented for the two short and two long wavelength bands, respectively.

Table 1: Hardware Specifications of the Far-Infrared Surveyor (FIS)

Photometric mode				
Band	N60	WIDE-S	WIDE-L	N160
Wavelength Range (μm)[1]	50–80	60–110	110–180	140–180
Band Centre (μm)	65	90	140	160
Band Width (μm)[2]	21.7	37.9	52.4	34.1
Detector	Monolithic Ge:Ga[3]		Stressed Ge:Ga	
Array size	20×2	20×3	15×3	15×2
Operational Temperature	~ 2.0 K		~ 2.0 K	
Pixel size (arcsec)[4]	26.8		44.2	
Pixel pitch (arcsec)[4]	29.5		49.1	
Readout	Capacitive Trans-Impedance Amplifier (CTIA)			
Sampling rate (Hz)	25.28		16.86	

[1] The detector responsivity is higher than 20% of the peak.
[2] See Section 3.1 for definition.
[3] The SW detector was manufactured by NICT.
[4] The real detector pixel shape projected on the sky show distortion from the optics.

Figure 1 shows the RSRFs (Relative Spectral Response Functions) of the four FIS photometry bands, composed from the pre-flight measurements. The RSRFs are given in the energy dimension and normalized at the band centre.

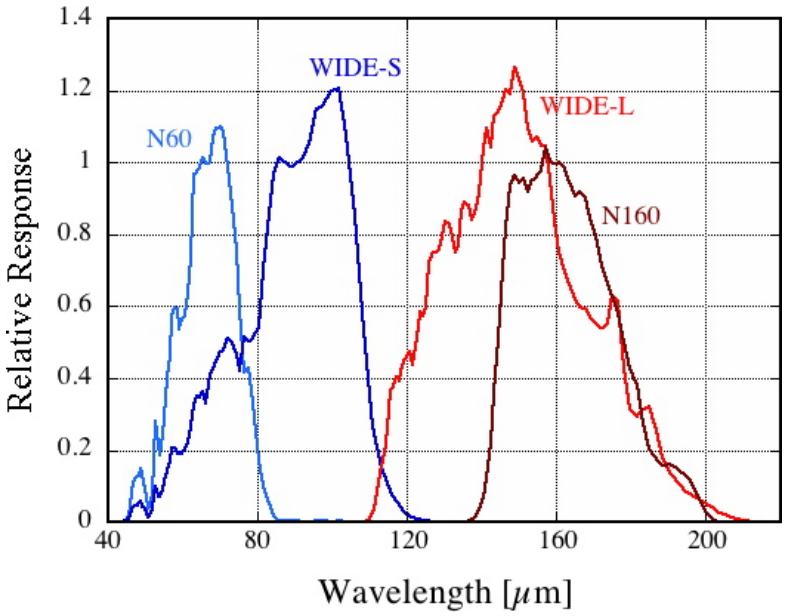

Figure 1: The RSRF (Relative Spectral Response Function) of the four FIS photometric bands normalized at the band centre of each band.

1.2.1 Data acquisition

The FIS detector system employs a CTIA (Capacitive Trans-Impedance Amplifier) readout circuit. The detector elements convert the incoming photons to current. The charge accumulated in the condenser in the back-end circuit is continuously read out with a constant rate (integration ramp). The charge is reset every fixed interval (0.5/1.0/2.0 sec). A suitable reset interval was estimated in the operational command generation from the expected sky brightness. This is the default sampling mode used for the survey observations. In this document we call this mode the *Normal* mode[2] In fact, real detector sampling is made at a higher rate, then every six samplings are summed onboard and recorded in the telemetry. This can reduce the noise by a factor of $\sim \sqrt{6}$ while preserving the data size. Therefore this mode is also referred to as the *coadd* mode.

The *CDS* (Correlated Double Sampling) mode is designed to avoid saturation in very bright regions, and was adopted when the survey scan was passing the inner galactic plane or other known very bright sources. The detectors are reset at every two samplings, and onboard differentiation of these two samplings is retrieved as the signal. Therefore, the downlinked data is already differentiated.

More details about the instruments and its characteristics are explained in the FIS Data Users Manual (Verdugo et al. 2007).

[2]The mode is called the *Nominal* mode in Observers Manual and Data Users Manual. We apologize for inconsistency.

2 Outline of data processing

2.1 Data reformatting

The first part of the AKARI All-Sky Survey data processing is to reformat of the data from satellite telemetry to the format suitable for data processing. FIS observation data and instrument status, Attitude and Orbital Control System (AOCS) data, and the house keeping data (temperature of the focal-plane instruments, telescope, and cryostat), were extracted from the telemetry packet and reconfigured in a simple two-dimensional table. The data format is called Time-Series Data (TSD) and is stored in FITS files. Each onboard instrument has different sampling timing and frequency. To make the data reduction software simple, we resampled the data to a unique sampling timing, namely that of the FIS detector. As the SW and LW detectors have different sampling frequencies, two files are produced per observation period. In addition to the data extracted from the telemetry, the scan position reanalysed on the ground (pointing reconstruction data; see Section 2.2), satellite positions in the Geocentric coordinates, and flags to indicate satellite day/night, the satellite being near by the Moon, and the SAA passage are implemented.

Since the FIS data acquisition was continuous, TSD data files are produced for every one hour length. The data files are maintained by the database, called Local Data Server (LDS). Users are able to access to the data in any continuous time range or sky area via LDS.

Details of the TSD format and software interface are discussed in the FIS Data Users Manual (Verdugo et al. 2007).

2.2 Pointing reconstruction

The pointing reconstruction, determination of the scan position during the survey, is carried as described here. There are two major steps; the first is the determination of the satellite attitude based on the attitude control sensors, and the second is to determine the telescope axis with the focal-plane sensors.

Information about the satellite attitude determined by the onboard computer is stored in the AOCS telemetry, together with the data from the AOCS sensors. The Ground-base Attitude Determination System (G-ADS) works with these data. Onboard ADS and G-ADS data are similar to each other, as they are based on the same sensor data, however, G-ADS processing should be more reliable since it uses both the past and future information, with sophisticated software including various corrections of the instrumental effects.

The remaining major source of uncertainty is the alignment between the AOCS system and the telescope axis, and its time variation. This is solved by the pointing reconstruction processing. The AKARI team in the ESA's European Space Astronomy Centre (ESAC) is in charge of this processing. The software system *PRESA* has been developed in a dedicated process for the AKARI All-Sky Survey pointing reconstruction. Input data are the G-ADS attitude, ephemeris data, Focal-plane Star Sensor (FSTS) scan data, and the IRC All-Sky Survey detection event list. The output returned from the processing are the survey attitude information and the identification list of the IRC events.

The data used for the current version FIS catalogue was processed by the PRESA version 3.4 in February 2009. The G-ADS data used for the processing is version "20081216m", with improved stableness and smoothness especially near the maneuvers. The IRC event list are the version produced in January 2009. See AKARI/IRC Point Source Catalogue Release Note for details. Figure 2 demonstrates the performance of the position information from *PRESA*. The plot shows fraction of the IRC events with error smaller than the given values. The error is the distance between the positions determined from the pointing reconstruction results and those from the position reference catalogue. For fair evaluation, the pointing reconstruction for this

test was carried out using randomly selected sources amounting to half of the catalogue, then the positions of the sources from the other half catalogue are determined for the evaluation. The error includes the pointing reconstruction processing error and the measurement error. For the brightest sources the measurement error should have minor contribution, and we can conclude that the position accuracy is better than 2.5 arcsec in 95 per cent of the events (c.f., original requirement was 3 and 5 arcsec in the in- and cross-scan direction in the final version). The position accuracy is also evaluated in the IRC Point Source Catalogue (Kataza et al. 2009). The mean angular separation between AKARI and 2MASS coordinates of the same sources is 0.765 ± 0.574 arcsec (*rms* from 720,942 measurements). Nearly 95 per cent of the sources have an angular separation < 2 arcsec and about 73 per cent have a separation < 1 arcsec. Note that these statistics were made for the number of IRC events or sources, and not for the sky area (or scan length).

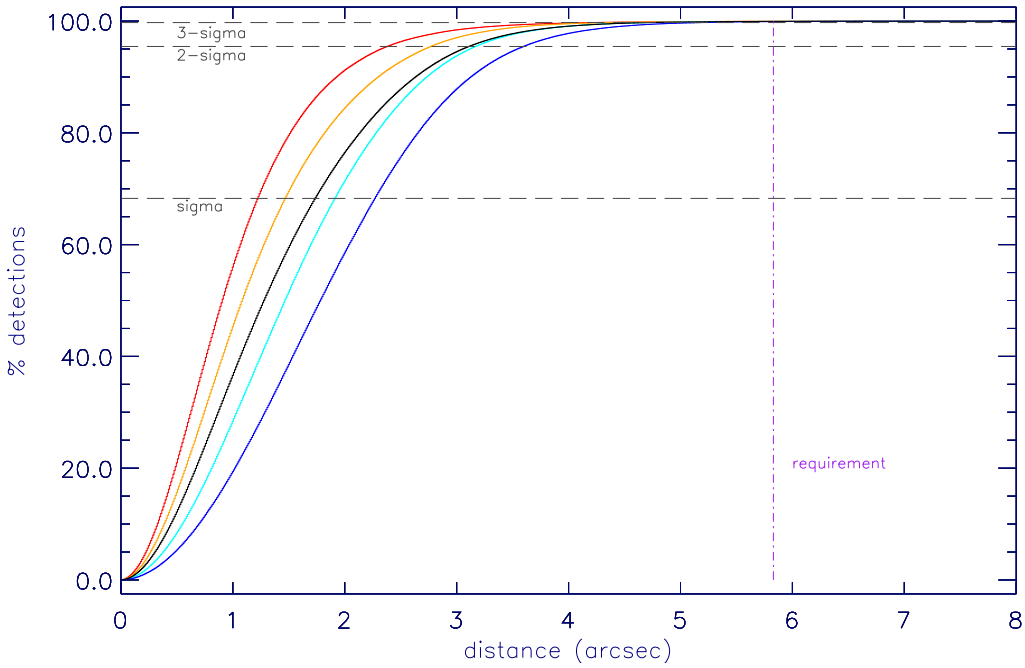

Figure 2: Error statistics of the pointing reconstruction data. The lines show the fraction of the IRC events with errors smaller than given values. Colours indicates different flux levels; Black: all sources, Red: F_ν at 9 μm > 0.7 Jy, Orange: 0.7 Jy $\geq F_\nu > 0.2$ Jy, Cyan: 0.2 Jy $\geq F_\nu > 0.1$ Jy, and Blue: 0.1 Jy $> F_\nu$. The error is estimated as the distance between the positions determined from the pointing reconstruction results and those from the position reference catalogue. The measurement error of the IRC events is also included. We see that more than 95 per cent of the bright events have positions more accurate than 2.5 arcsec.

2.3 *GreenBox*: Correction and calibration of scan data

The second stage of the pipeline, usually referred to as the *GreenBox*, consists of various processes to correct instrumental anomalies, to mask out bad data, and to calibrate the time sequence of the detector signal. Most of the processes are adopted to each pixel independently. Figure 3 presents the process flow in the *GreenBox*. Following major processes are included (indicated by the module names):

gb_conv_to_volt Readout signal from the detector in ADU is converted to Volt considering small non-linearity in the A/D converter.

gb_ramp_curve_corr In the *Normal* sampling mode the detector readout signal is the integrated charges in the backend circuit. The integrated signal (ramp curve) deviates from the linear relation with the sum of the incoming photons. The module correct the ramp curve to be proportional to the total incoming photon. The correction factor is derived from the special measurement under the constant flux from the calibration lamp. Small time variation of the ramp curve during the observation is observed as the periodic pattern in the scan data after the correction.

gb_differentiation The ramp curve signal is differentiated so that the data should represent the sky brightness. Current pipeline takes simple subtraction from the previous sampling point.

gb_periodic_noise Electrical interference from the external noise source to the readout circuit appears as noise with slowly time varying frequency (In fact what we see in the data is the beating of several higher frequency noises). The noise appears coherently in all pixels. The interference of this noise to the signal is much more prominent in the SW detectors. The module applies sine-wave fitting and subtraction. The noise component is reduced by up to a factor of few.

gb_set_glitch_status_mmt Charged particles hit the detector producing strong and spiky signal changes. Often temporary responsivity changes follow. These non astronomical rapid changes of the signal are called 'glitches'. The module detects glitches and masks them not to be used in the following processing.

gb_detect_flutter Very heavy glitches sometimes make the detector unstable and disturbed signals last for tens of minutes. It usually appears per detector. This phenomenon is called 'flutter' from its signal variation pattern. This module detect the flutter signal pattern following the big glitches, and masks the data until the detector signal gets back to be stable.

gb_dark_subtraction, gb_dc_responsivity_corr Time varying dark level and detector responsivity are corrected by monitoring shutter close data / calibration lamp pulse data. After these processing the detector signal in the TSD data is supposed to be proportional to the sky brightness. Absolute calibration is not applied in this stage (**gb_flux_calib** is not actually working).

gb_reintegration This procedure is added as a preparatory processing at the source extraction. The detector readouts in the *GreenBox* output scan data are integrated, then again differentiated such a way that every three data points are fitted with two-order polynomial and the tilt at the middle point is calculated. This process reduces the noise level ideally by $\sqrt{2/3}$ from the default simple subtraction.

2.4 Source Extraction

Source extraction and photometry were carried out by *SUSSEXtractor* (hereafter *SXT*) developed for the AKARI/FIS All-Sky Survey by the team in University of Sussex. The software applies Bayesian statistics in the source detection process. Details of the general algorithm of the source detection is described in Savage & Oliver (2007).

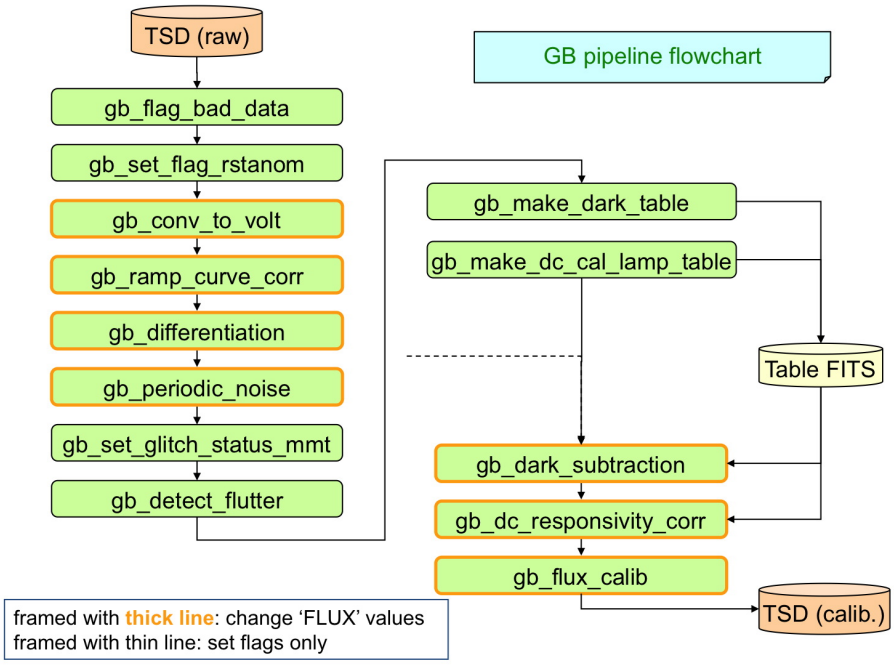

Figure 3: Process flow in the *GreenBox* part of the data reduction pipeline.

In Bayesian statistics a value called the "evidence" is used to represent the probability of the assumption. In our case, this value indicates how likely the sky brightness distribution can be explained by combination of a point source and background sky, rather than a simple sky without source. In the catalogue, evidence is presented in logarithmic form and is referred to as *logEvidence*.

The sky is divided into 3×3 deg^2 regions in the Ecliptic coordinate (as the survey scan is approximately along the Ecliptic meridian) and source extraction process is applied per this unit sky. At the high Ecliptic latitude region a region covers wider longitude ranges. The actual set of scan data covers slightly larger sky region (3.5×3.5 deg^2). to assure enough size of the background for any sources in the region. After the processing only those sources inside the defined region are considered. The source extraction consists of the following procedures.

Each region was typically covered by one hundred scans (minimun 44 to maximum almost 3500 depending on the Ecliptic coordinates). They are grouped so that the scans in each group cover the sky as uniformly as possible with minimum overlaps and gaps. Also, a group consists with scans taken in a period within a month (usually less than a week except for polar regions).

2.4.1 Source detection

All available scan data in the region are added up into a sky map (coadd map) and source detection is applied to it. A detection list (source candidate list) is the output of this process. The source detection process is currently only made in the WIDE-S band, as the band is far more sensitive than other three bands. On the other hand we might miss some very bright sources because of detector saturation etc. (See Section 7.5).

Sources are found as a local peaks on the *logEvidence* map of the region with the value larger than the given threshold. A unique peak is searched in a circle of 48 arcsec radius. So

the minimum distance between sources is no smaller than 48 arcsec.

2.4.2 Photometry and astrometry

We measure the *flux*, *logEvidence* and other quantities at each position on the detection list in all four bands. The flux measurement is made on the coadd data, which is referred to in the catalogue. Measurements on the grouped scan data are also carried out to evaluate the flux measurement error. In the current processing we simply measure the quantities at the positions in the detection list. No further tuning of the source positions is not attempted.

2.4.3 Hours confirmation

Sources are regarded as *real* when *logEvidence* exceeds the threshold in the coadd data as well as in more than two groups (scans), and also in more than 3/4 of the total number of groups observed that position. The flux and number of data samplings contributed to the measurement are also considered, to discard bad quality data. This is referred to as *Hours confirmation*. Two values, *NSCANC* and *NSCANP* in the catalogue, holds the information of number of detected and observed groups.

A source is "Months confirmed" if it is detected in the scan groups separated more than one month (in most cases a source can only be visible for days in every half year but longer in the polar regions). The flag *MCONF* is set for the corresponding sources.

There is no *seconds confirmation* in the processing. This is because that the signals on the adjacent pixels in the FIS detectors, especially on the SW detector, are not always independent due to the monolithic structure of the array. A glitch sometimes appears two or more pixels next to each other. On the other hand thanks to the high spatial resolution and accurate position information *Hours confirmation* works very effectively to confirm real sources.

2.4.4 Band merging

Source measurements and confirmation are carried out in each FIS band and per readout mode. After all of the processing, band merging is carried out; astronomically useful information is extracted and merged into a catalogue file.

As the measurements in four bands are made at the same position given in the detection list, identification between different wavelength data is simple and secure. Some sources near the Galactic plane were observed both in the *Normal* and *CDS* modes. In such case we take one of two of the following rules; (1) take one with larger *logEvidence* $\times$ *weight*, where weight is 3 for confirmed sources and 1 for non-confirmed ones. (2) if two measurements have the same value, we take the one with larger *NSCANC* (number of confirmed scans), (3) otherwise take the *Normal* mode data. All conditions prefer to use *Normal* mode data than *CDS*.

3 Flux Calibration

3.1 Conversion from data unit to astronomical unit

The point source flux density in the FIS photometry is defined by the following equation:

$$F_\nu(\nu_c)\Delta\nu = \int F_\nu(\nu)R(\nu)d\nu. \quad (1)$$

Where $F_\nu(\nu_c)$ is the source flux at the central wavelength (that appears in the catalogue). $R(\nu)$ is the Relative Spectral Response Function (RSRF; Figure 1) defined for energy dimension. $\Delta\nu$ is the band width defined for the constant energy spectrum $\nu\mathcal{F}_\nu = \text{const.}$;

$$\Delta\nu \equiv \int \mathcal{F}_\nu(\nu)R(\nu)d\nu \Big/ \mathcal{F}_\nu(\nu_c)R_\nu(\nu_c). \quad (2)$$

These definitions should be consistent with IRAS and previous missions.

Flux in the current version catalogue is measured on the coadd map (from all available scan data). Conversion factors from the photometry measurements in ADU to the astronomical unit in Jy is derived by comparing the model flux and measurements during the survey. Three kinds of objects are used; the stellar calibrators (Cohen et al. 1999; 2003b; 2003b), the asteroids (Müller & Legerros 1998; 2002) and the planets Uranus and Neptune (Moreno 2007).

The upper panel of a pair of plots per band in Figure 4 shows the conversion factors (measured signal divided by the model flux) for every reference sources versus their measured signal. Only high quality observations are included in the analysis. We see that the conversion factor depends on the source flux. To simplify the problem we apply one-dimensional polynomial fits to the relation of log Flux versus conversion factor. The conversion factors for the four bands are given by the following formulae:

N60:	$S/F = +0.71146 + 0.05669 \times \log(S)$
WIDE-S:	$S/F = +2.75829 + 0.41886 \times \log(S)$
WIDE-L:	$S/F = +8.05248 + 1.12364 \times \log(S)$
N160:	$S/F = +20.14181 - 2.85792 \times \log(S)$

Here F is the source flux in [Jy] and S is the measured signal in ADU.

The lower panels of the plots in Figure 4 show the ratio of the calibrated flux using the derived formulae to the model flux. Scatter around 1.0 indicates the uncertainty of the absolute flux calibration. We regard the standard deviation of the scatter as the uncertainty of the absolute calibration, since any choice of the calibration reference changes the conversion factor to that level. We further round the numbers and conclude that the uncertainties are 15 per cent for all the FIS bands. The actual flux error in the catalogue is also affected by the errors in each measurement, as discussed in Section 5.3.

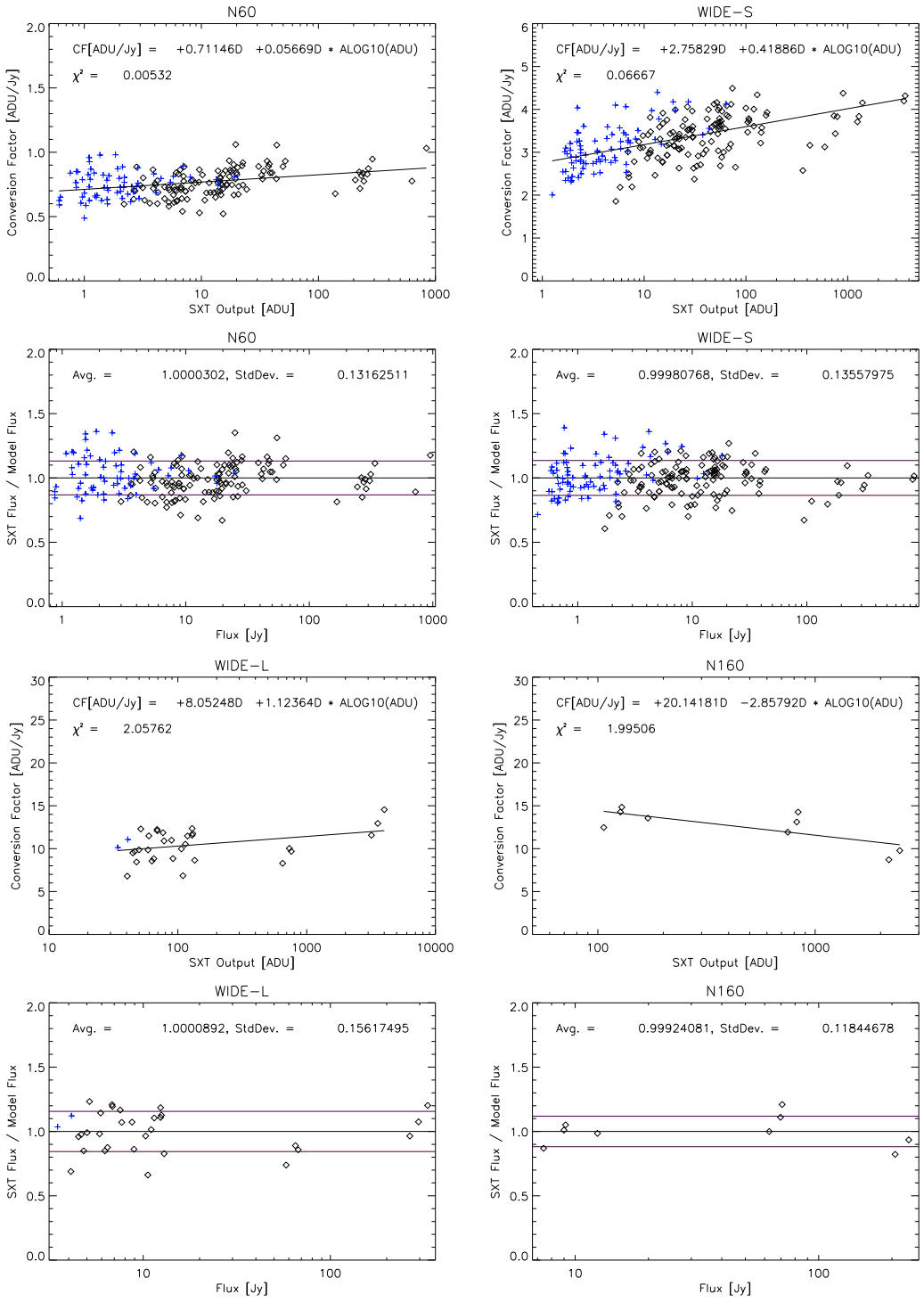

Figure 4: The absolute calibration for point sources in the four FIS bands. N60 (a pair of plots in top-left), WIDE-S (top-right), WIDE-L (bottom-left), and N160 (bottom-right), respectively. The upper panel of each pair of plot shows the conversion factor (the ratio of SXT measured flux in ADU divided by the model flux in Jy) from each observation for their SXT flux. Both stellar (blue crosses) and solar system calibrators (black diamonds) are used except for N160 that does not have good quality measurements of any stellar calibrators. The best fit line to these data is the flux dependent conversion formula. The lower panel shows ratio of 'calibrated flux' to the model flux.

3.2 Flux calibration for the *CDS* mode data

The *CDS* (Correlated Double Sampling) mode was used to observe bright sky regions such as the inner Galactic-plane to avoid saturation. Due to reduced exposure times and frequent resets the sensitivity of the *CDS* mode data is about one order of magnitude worse than that of the *Normal* mode. Unfortunately, no reliable calibration source was observed in the *CDS* mode. Calibration of the *CDS* mode data was carried out by relative manner from the *Normal* mode data. There are some sources that happened to be observed in both the *CDS* and the *Normal* mode. We compare the SXT output signal from both mode for sources brighter than the *CDS* mode detection limit to derive a correction formula for each band. Measurements in the *CDS* mode were translated to the corresponding ADU in the *Normal* mode, then the unique correction from ADU to Jy is applied. Figure 5 displays the comparison of two sampling modes and fitting results. The correction factor for each band is given as the following formulae:

$$\text{WIDE-S:} \quad S_{\rm CDS}/S_{\rm Normal} = +1.89560 - 0.08689 \times \log(S_{\rm CDS})$$

$$\text{N60:} \quad S_{\rm CDS}/S_{\rm Normal} = +1.21551 + 0.04558 \times \log(S_{\rm CDS})$$

$$\text{WIDE-L:} \quad S_{\rm CDS}/S_{\rm Normal} = +0.90698 + 0.13500 \times \log(S_{\rm CDS})$$

$$\text{N160:} \quad S_{\rm CDS}/S_{\rm Normal} = +0.42951 + 0.28822 \times \log(S_{\rm CDS})$$

The flux dependency of the correction factor can be understood from the non-linear characteristics of the ramp curve.

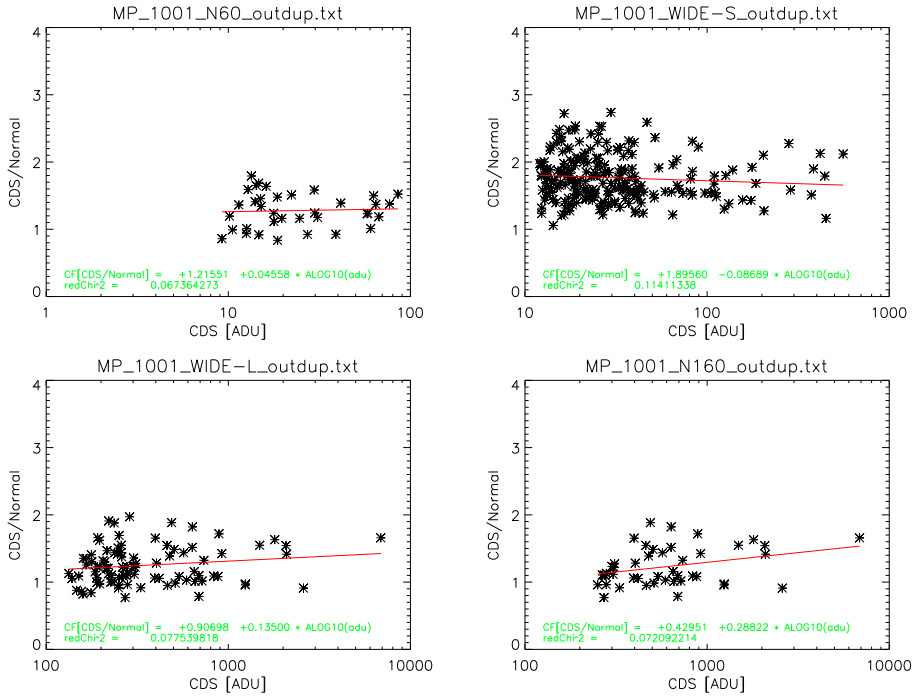

Figure 5: The *CDS* and *Normal* mode SXT measured signals from the same sources are compared in the ADU scale. The ratio of both data mode gives the correction factor. We see slight dependency of the ratio to the flux. Sources fainter than the expected *CDS* detection limit are excluded in the analysis. Note that the sources are mostly along the Galactic plane.

3.2.1 Colour correction

Since the FIS photometry bands are broad wavelength coverage, colour correction is needed for detailed analysis. The colour correction factor K is given by;

$$K = \frac{\int F(\nu)R(\nu)d\nu}{F(\nu_c)} \Big/ \frac{\int F_{\rm flat}(\nu)R(\nu)d\nu}{F_{\rm flat}(\nu_c)}, \tag{3}$$

where $F_{\rm flat}$ is the constant energy spectrum $\nu F_{\rm flat}(\nu) = {\rm const.}$, $F(\nu)$ is the source spectrum, and $R(\nu)$ is the RSRF.

Table 2 gives the colour correction factors ($K = F_{\rm catalogue}/F_{\rm real}$) for various spectral energy distribution (taken from Table 9. of Shirahata et al. 2009).

Table 2: Color correction factors. Taken from Table 9. of Shirahata et al. (2009)

Intrinsic spectrum	*N60* (65 μm)	*WIDE-S* (90 μm)	*WIDE-L* (140 μm)	*N160* (160 μm)
Black-body[1] ($\beta = 0$)				
$T = 10$	4.434	1.840	1.549	1.097
$T = 30$	1.050	0.892	0.957	0.986
$T = 50$	0.976	0.979	0.937	0.986
$T = 70$	0.978	1.066	0.935	0.988
$T = 100$	0.992	1.154	0.935	0.989
$T = 300$	1.029	1.320	0.936	0.992
$T = 1000$	1.044	1.381	0.937	0.993
$T = 3000$	1.048	1.398	0.937	0.993
$T = 10000$	1.049	1.404	0.937	0.993
Gray-body[1] ($\beta = -1$)				
$T = 10$	5.248	2.093	1.770	1.143
$T = 30$	1.107	0.902	0.999	0.994
$T = 50$	0.997	0.935	0.962	0.989
$T = 70$	0.983	0.986	0.953	0.989
$T = 100$	0.985	1.041	0.949	0.989
$T = 300$	1.005	1.148	0.945	0.990
$T = 1000$	1.013	1.187	0.944	0.990
$T = 3000$	1.016	1.198	0.943	0.990
$T = 10000$	1.016	1.202	0.943	0.990
Gray-body[1] ($\beta = -2$)				
$T = 10$	6.281	2.396	2.048	1.198
$T = 30$	1.178	0.930	1.060	1.008
$T = 50$	1.030	0.918	1.003	0.998
$T = 70$	1.001	0.944	0.987	0.995
$T = 100$	0.992	0.976	0.978	0.994
$T = 300$	0.995	1.041	0.968	0.993
$T = 1000$	0.999	1.065	0.965	0.992
$T = 3000$	1.000	1.072	0.964	0.992
$T = 10000$	1.001	1.075	0.964	0.992
Power-law[2]				
$\alpha = -3$	1.040	0.954	1.129	1.033
$\alpha = -2$	1.013	0.962	1.054	1.013
$\alpha = -1$	1.000	1.000	1.000	1.000
$\alpha = 0$	1.001	1.076	0.964	0.992
$\alpha = 1$	1.017	1.203	0.943	0.990
$\alpha = 2$	1.049	1.407	0.937	0.993
$\alpha = 3$	1.101	1.724	0.945	1.001

Note.
[1] Gray-body spectrum : $F(\nu) \propto B_\nu(T) \cdot \nu^\beta$.
[2] Power-law spectrum : $F(\nu) \propto \nu^\alpha$.

4 Catalogue contents and format

4.1 Catalogue format

The contents and format of the FIS Bright Source Catalogue Version 1 is summarized in Table 3. The catalogue will be distributed in three ways; a FITS file, a text file, and access via *AKARI Catalogue Archive Server (AKARI-CAS)*.

Table 3: Catalogue contents, formats and short descriptions. Type is for the FITS data, and Format and Column for the Text formatted file.

Keyword	Type	Format	Column	Short description
OBJID	Long	I10	1–10	Internal Object ID
OBJNAME	String	A15	11–25	Source identifier
RA	Double	F10.5	26–35	Right Ascension (J2000) [deg]
DEC	Double	F10.5	36–45	Declination (J2000) [deg]
POSERRMJ	Float	F6.2	46–51	Position error major axis [arcsec]
POSERRMI	Float	F6.2	52–57	Position error minor axis [arcsec]
POSERRPA	Float	F6.1	58–63	Position error Position Angle [deg]
FLUX65	Float	E11.3	64–74	Flux density in N60 [Jy]
FLUX90	Float	E11.3	75–85	Flux density in WIDE-S [Jy]
FLUX140	Float	E11.3	86–96	Flux density in WIDE-L [Jy]
FLUX160	Float	E11.3	97–107	Flux density in N160 [Jy]
FERR65	Float	E10.2	108–117	Flux uncertainty in N60 [Jy]
FERR90	Float	E10.2	118–127	Flux uncertainty in WIDE-S [Jy]
FERR140	Float	E10.2	128–137	Flux uncertainty in WIDE-L [Jy]
FERR160	Float	E10.2	138–147	Flux uncertainty in N160 [Jy]
FQUAL65	Integer	I2	148–149	Flux density quality flag for N60
FQUAL90	Integer	I2	150–151	Flux density quality flag for WIDE-S
FQUAL140	Integer	I2	152–153	Flux density quality flag for WIDE-L
FQUAL160	Integer	I2	154–155	Flux density quality flag for N160
FLAGS65	Integer	Z5	156–160	Bit flags of data quality for N60
FLAGS90	Integer	Z5	161–165	Bit flags of data quality for WIDE-S
FLAGS140	Integer	Z5	166–170	Bit flags of data quality for WIDE-L
FLAGS160	Integer	Z5	171–175	Bit flags of data quality for N160
NSCANC65	Integer	I5	176–180	nScanConfirm for N60
NSCANC90	Integer	I5	181–185	nScanConfirm for WIDE-S
NSCANC140	Integer	I5	186–190	nScanConfirm for WIDE-L
NSCANC160	Integer	I5	191–195	nScanConfirm for N160
NSCANP65	Integer	I5	196–200	nScanPossible for N60
NSCANP90	Integer	I5	201–205	nScanPossible for WIDE-S
NSCANP140	Integer	I5	206–210	nScanPossible for WIDE-L
NSCANP160	Integer	I5	211–215	nScanPossible for N160
MCONF65	Integer	I3	216–218	Months confirmation flag for N60
MCONF90	Integer	I3	219–221	Months confirmation flag for WIDE-S
MCONF140	Integer	I3	222–224	Months confirmation flag for WIDE-L
MCONF160	Integer	I3	225–227	Months confirmation flag for N160
NDENS	Integer	I4	228–231	Number of neighbouring sources

4.2 Description of the catalogue contents

OBJID

A unique number for each object in the catalogue. This is mostly for internal use in the AKARI-CAS, and should be ignored in the astronomical analysis.

OBJNAME

Source identifier from its J2000 coordinates, following the IAU Recommendations for Nomenclature (2006). The format is HHMMSSS+/−DDMMSS, e.g., 0123456+765432 for a source at (01h23m45.6s, +76d54m32s). **The source must be referred to in the literatures by its full name; AKARI-FIS-V1 J0123456+765432**.

RA, DEC

J2000 Right Ascension and Declination of the source position in degree.

POSERRMJ, POSERRMI, POSERRPA

One-sigma error of the source position expressed by an ellipse with Major and Minor axes in arcsec, and Position Angle in degees measured from North to East. In the currently version we give the same value (6.0 arcsec) for all the sources both in the major and minor axis (thus polar-angle is 0.0) based on the statistical analysis in Section 5.5.

FLUX65, FLUX90, FLUX140, FLUX160

Flux density of the source in the four FIS bands in Jansky. In the catalogue the four FIS bands are indicated by their central wavelengths as 65, 90, 140 and 160.

Values are given even for the unconfirmed sources as much as possible, though such the data are not guaranteed. If it is not possible to measure the source flux, *NULL* value is set; *NaN* in the FITS format and −999.9 in the text format, respectively.

FERR65, FERR90, FERR140, FERR160

Flux uncertainty of the source flux in Jansky. It is evaluated as the standard deviation of the fluxes measured on the individual scans divided by the root square of the number of measurements (presented in *NSCANC*). The error thus only includes relative uncertainty at the measurements. Details of the flux uncertainty are discussed in Section 5.3.

When it is not possible to calculate the standard deviation, *NULL* is set to this column. The text version has −99.9.

FQUAL65, FQUAL90, FQUAL140, FQUAL160

Four level flux quality indicator:

3: High quality (the source is confirmed and flux is reliable)
2: The source is confirmed but flux is not reliable (see FLAGS)
1: The source is not confirmed
0: Not observed (no scan data available)

FLAGS65, FLAGS90, FLAGS140, FLAGS160

A 16 bits flag per band indicating various data condition. In version 1 catalogue three bits are used. The first bit (bit0) is used to indicate the *CDS* sampling mode. The second bit (bit1) warns the flux of the band is less than a half of the detection limit, and is not reliable. The fourth bit (bit3) tells that the source is possibly false detection due to 'side-lobe' effects (see, Section 7.7). The third bit (bit2) was previously indicated an anomaly which does not exist in the current version, and thus is kept unused. Sources with bit1 or bit3 = 1 have $FQUAL = 2$ or less. Other bits are reserved for the future implementation. In the text format version the values are expressed in Hexadecimal format.

```
                                USB ------------- bit ----- LSB
                                    ... 7  6  5  4  3  2  1  0
                                decimal |  |  |  |  |  |  |  |
reserved ------------------------- 128--+  |  |  |  |  |  |  |
reserved -------------------------- 64 ----+  |  |  |  |  |  |
reserved -------------------------- 32 -------+  |  |  |  |  |
reserved -------------------------- 16 ----------+  |  |  |  |
1: possibly 'side-lobe' detection--- 8 -------------+  |  |  |
not used ------------------- ------- 4 ----------------+  |  |
1: Flux too low ------------------- 2 -------------------+  |
0: Normal mode, 1: CDS mode -------- 1 ----------------------+
```

x *NULL* is set in case of no measurement ($FQUAL = 0$). The value is -1 in the files, and is defined as *NULL* in the FITS header.

NSCANC65, NSCANC90, NSCANC140, NSCANC160

Number of scans on which the source is properly detected with *logEvidence* larger than the threshold.

NSCANP65, NSCANP90, NSCANP140, NSCANP160

Total number of scans that passed on the source (that possibly observed the source)

MCONF65, MCONF90, MCONF140, MCONF160

The month confirmation flags are prepared per band. The value is 1 when the source is observed in the scans separated more than one months (usually an object is visible at every 6 months). This information is independent to hours confirmation and can be 1 even if the source is not confirmed ($FQUAL = 1$). Because of the visibility constraint of the AKARI Survey, some sky regions were observed by scans only within a month. *MCONF* = 0 does not mean that the source is unreliable.

This flag is *NULL* (-1) for $FQUAL = 0$ sources.

NDENS

Number of sources in the catalogue within the distance of 5 arcmin from the source. This value is intended to be an indicator of crowdedness of the sky region. Since the source extraction program is tuned so that a unique source is found within 48 arcsec radius, the 5 arcmin radius corresponds to approximately 40 beams.

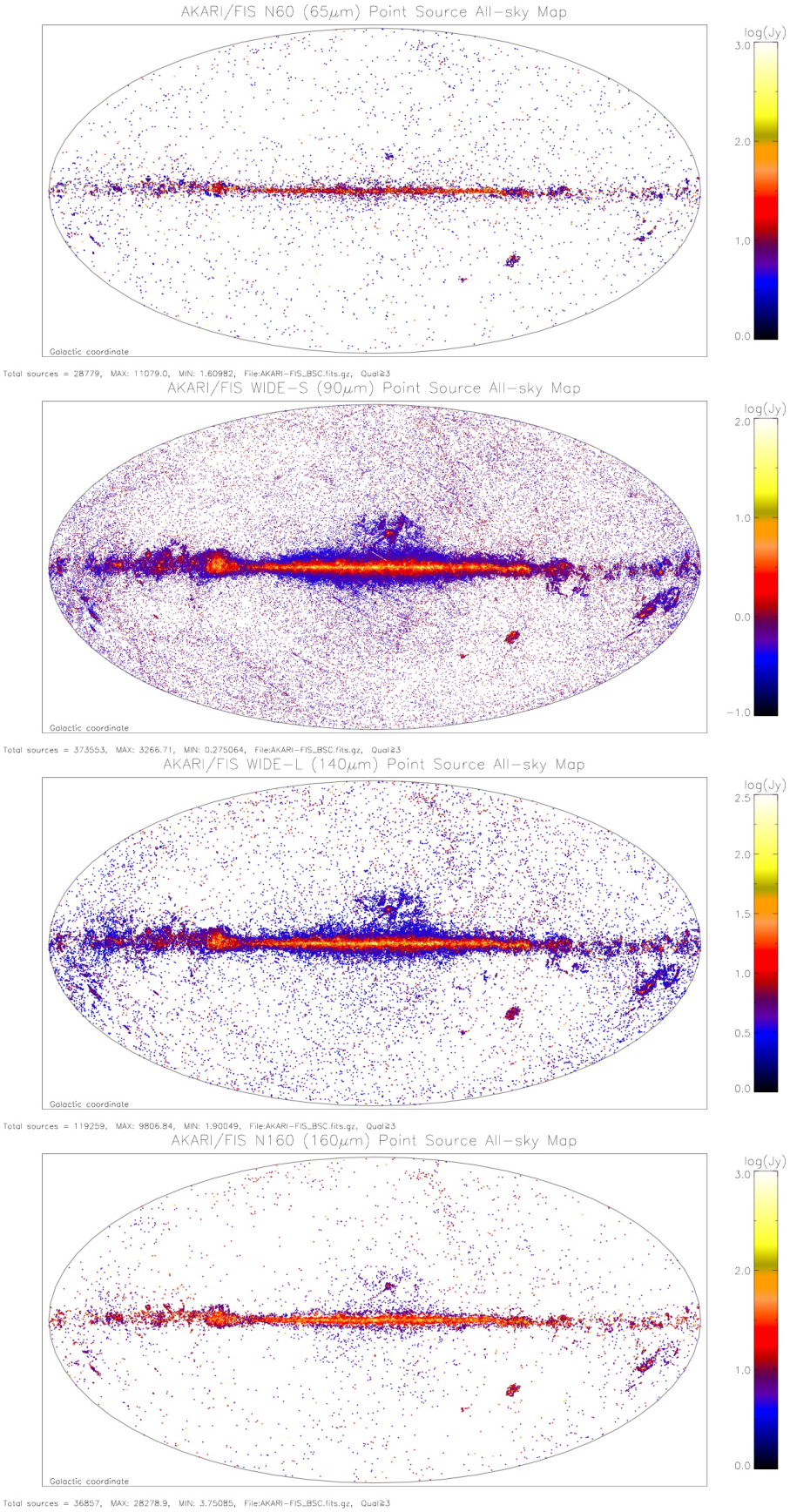

Figure 6: Sky distribution of the detected sources. From top to bottom; N60, WIDE-S, WIDE-L, N160.

5 Performance

In the following sections we show the performance of the current catalogue in a statistical manner so that users can understand the availability and limitations of the data.

5.1 Number of sources

As we describe in Section 2.4 the source detection is carried out in the most sensitive band, WIDE-S, then the measurements at the positions were attempted in the all four bands. The catalogue includes any sources confirmed at least one of the wavelength bands. Sources that are confirmed at the band are indicated by the quality flag $FQUAL = 3$. Sources those are confirmed, but might have problem are degraded to $FQUAL = 2$. Two reasons are currently considered; sources with too low flux level, and possible false detections due to 'side-lobe' effect. Flux at the source position on the coadd map is given as much as possible even for the bands in which the source is unconfirmed ($FQUAL = 1$), but the value may be unreliable. Users are recommended NOT to use the data of unconfirmed sources for reliable scientific analysis. In Table 4 we list the number of sources in the four bands.

Table 4: Number of sources in the current catalogue.

		FQUAL=3		*FQUAL*=2	*FQUAL*=1	*FQUAL*=0
Band	Total	*Normal* mode	*CDS* mode			
N60	28779	10799	17980	1836	394746	1710
WIDE-S	373553	250804	122749	10934	42573	11
WIDE-L	119259	66276	52983	5851	301566	395
N160	36857	14722	22135	2451	386192	1571
Total number of sources = 427071						

Figure 7 shows $\log N - \log S$ plots of the confirmed sources in the current catalogue. Data taken in the *Normal* and *CDS* modes are plotted in separate panels as they have different sensitivity. A few remarkable points are found in the plots. We see bumps near the peaks of the plots. It is especially noticeable in the WIDE-S band in the *Normal* mode. We suspect that they are due to "Eddington bias" (fluxes of faint sources just below the detection limit are overestimated as they are only observed when measurement error works to increase the flux). The possibility of detections by chance coincidences (noise peaks are recognized as sources) may be relatively low. Among 178,342 sources with 90 μm flux below 1.0 Jy, 127,810 sources are detected more than three scans, and 130,182 sources are $MCONF90 = 1$.

We find a certain fraction of sources below the detection limits in N60, WIDE-L and N160. As we describe in the previous section the photometry on these bands is based on the detection list in the WIDE-S band. We find that most of faint sources far below the detection limits are also faint in the WIDE-S band. Photometry of such faint sources are likely affected by noise, and use of these data for quantitative discussion is not recommend. These faint sources can be distinguished by $FQUAL = 2$ and a bit in *FLAGS*. See, Section 7.6.

Drops of numbers of the brightest sources are most probably due to detector saturation and incomplete deglitching.

Sky distributions of the detected sources are presented in Figures 6.

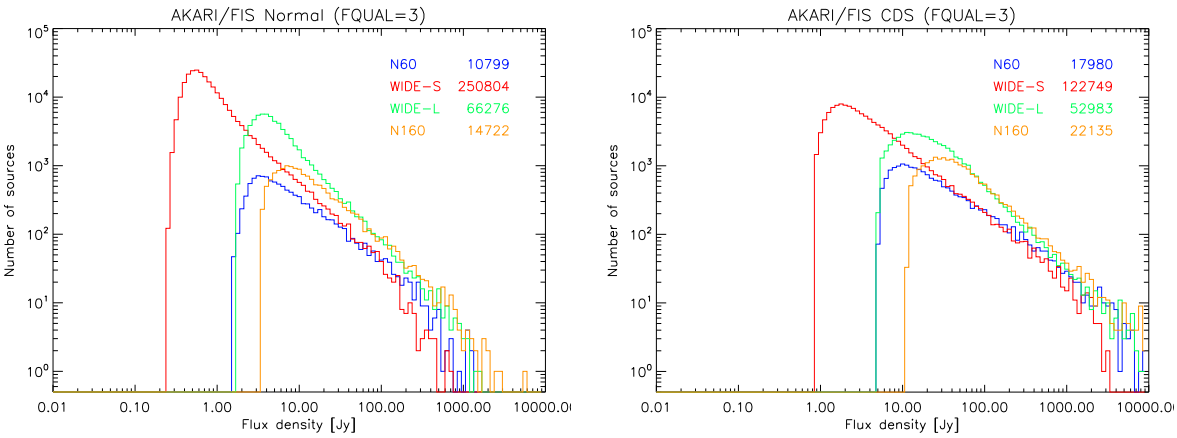

Figure 7: $\log N - \log S$ plots of the sources with $FQUAL = 3$. Four bands are indicated in different colours. Sharp edges at the low flux side are due to low-flux threshold described in Section 7.6.

5.2 Detection limits

Estimating the detection limit in each band of the AKARI-FIS catalogue is not an easy task as it may depend on the environment such as background level, readout mode, and glitch density etc. In the following subsections we describe two independent estimates of detection limits.

5.2.1 Completeness of detection using calibration stars

The completeness of the detection is evaluated using the calibration standard stars with known flux. As they are too faint for the LW bands, the analysis is only made for N60 and WIDE-S. The number of sources is not large especially in the high-flux range, but most of the cases, the statistics are accurate enough for estimating the detection limit.

Figure 8 shows the fraction of number of stars found in the catalogue to those must be detected, as a function of the fluxes. In general completeness (detection rate) increases rapidly at certain flux. From these plots we can estimate the detection limit (here defined as the flux where completeness exceeds 90 per cent) of the current catalogue is ~ 3 Jy for N60 and ~ 0.5 Jy for WIDE-S, respectively.

5.2.2 Peak flux of $\log N$-$\log S$ plot

Assuming that the source count function, i.e., the number of sources as a function of their flux, does not change drastically in the AKARI/FIS flux range we can say that the drop of number count at the faint end is due to the instrumental detection limit. Table 5 indicates peak fluxes in the $\log N$-$\log S$ plot (Figure 7) for the *Normal* mode and the *CDS* mode. The five-σ noise levels in the *Normal* sampling mode presented in Kawada et al. (2007) are also given as the references. Since the source detection is defined by *logEvidence* value, the detection limits may not be expressed by a constant n-σ. The peak fluxes on the $\log N$-$\log S$ plot are about 7, 5, 14, and 6-σ in N60, WIDE-S, WIDE-L and N160 bands, respectively. The *CDS* mode is generally 3–5 times worse than the *Normal* mode.

The values for the *Normal* mode in the table are well consistent with those from the completeness plot. Therefore, we conclude that the values in the Table 5 can be regarded as the detection limit of the current catalogue.

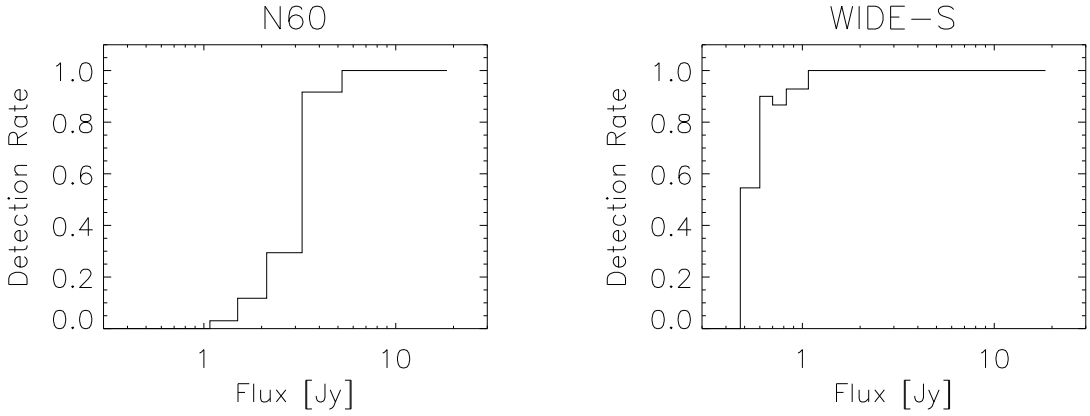

Figure 8: Detection completeness based on the stellar calibration sources with known flux.

Table 5: Peak flux of $\log N$-$\log S$ plot and five-σ noise levels per scan (in the *Normal* mode) in Kawada et al. (2007).

	Detection Limit		Kawada et al.
Band	*Normal* [Jy]	*CDS* [Jy]	5σ noise [Jy]
N60	3.2	11	2.4
WIDE-S	0.55	1.8	0.55
WIDE-L	3.8	11	1.4
N160	7.5	25	6.3

Applying the same assumption of source count function, we can estimate the completeness of detection, given in Table 6. The smaller flux than the detection limit is obtained for WIDE-S due to bump at lower end. On the other hand N160 band shows quite high flux for completeness = 100 per cent because of mild peak in the plot.

Table 6: Estimated detection completeness for the *FQUAL=3* sources with respect to the expected number of sources from the $\log N - \log S$ relation.

	Normal mode				CDS mode			
Completeness [%]	10	50	80	100	10	50	80	100
N60	1.9	2.6	3.3	5.2	5.5	7.2	10	17
WIDE-S	0.32	0.39	0.43	0.47	1.0	1.4	2.1	3.8
WIDE-L	2.0	2.9	3.6	4.3	6.2	13	22	32
N160	3.8	5.9	8.2	15	13	25	39	60

5.3 Flux uncertainty

There are in principle two sources of uncertainty of the flux given in the catalogue; the relative error at the photometry of each source and the absolute error from the uncertainty of the flux conversion factors. Table 7 summarizes the estimated total flux uncertainty of each band.

Table 7: Estimated flux uncertainty for bright sources

Band	Total	Relative	Absolute
N60	20 %	10 %	15 %
WIDE-S	20 %	10 %	15 %
WIDE-L	20 %	10 %	15 %
N160	20 %	10 %	15 %

The source of the relative error are noises, effects of glitches, residuals in responsivity correction, and other data anomalies. As the fluxes in the current catalogue are measured on the coadd image maps (from all available scans at the position), time variation of the objects' intrinsic intensity could also be a reason of scatter. Evaluation of time variation is an issue in the future version catalogue). The relative flux uncertainty in the present catalogue is estimated from the standard deviation of the flux measured on individual scans divided by root-square of the number of contributed scans, which represents the estimated error of the average value.

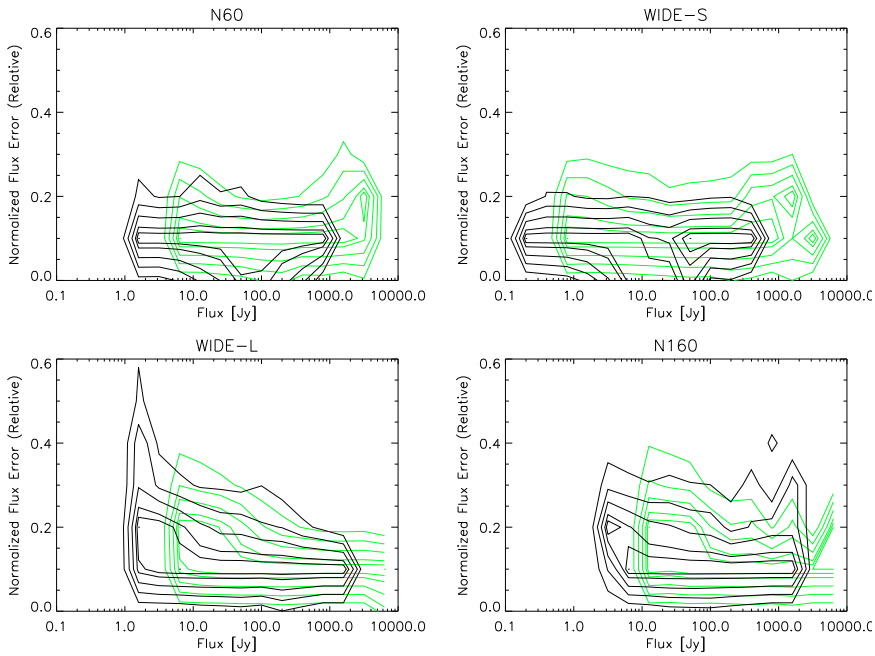

Figure 9: The number density coutours of sources with certain flux error. The density is normalized at each flux bin to give fair comparison between the flux levels. The coutours are at 0.2, 0.4, 0.6, 0.8, and 0.9. Black contours are for the *Normal* mode data and Green ones are for the *CDS* mode. We see that the majority of the sources have almost the same flux error of about 10 per cent regardless of their flux level. Only faint sources in WIDE-L and N160 have larger errors.

Plots in Figure 9 show the number density contour of the normalized flux error. Number density is normalized per each flux bin so that the peak of the contour indicates the relative flux error for the majority of the sources. The error is typically 10 per cent throughout the flux range in N60 and WIDE-S, and for the bright sources in WIDE-L and N160. This fact means that the major source of the error is not random noises, but rather the error in the responsivity correction. Only faint sources in WIDE-L and N160 bands show effects of random errors.

The sources of the absolute calibration uncertainty are errors in the model fluxes, errors in the relative spectral response functions (RSRFs), and measurement errors of the calibration reference sources. Following the discussions in Section 3.1, the uncertainty of the flux conversion factors is estimated as 15 per cent for all the bands.

5.4 Band-to-band flux comparison

Fluxes in the four AKARI bands are compared with each other in Figure 10. We see deviations from the limear relationship in the bright sources especially in the *CDS* mode. The brightest objects may be affected by saturation or incorrect deglitcing processes.

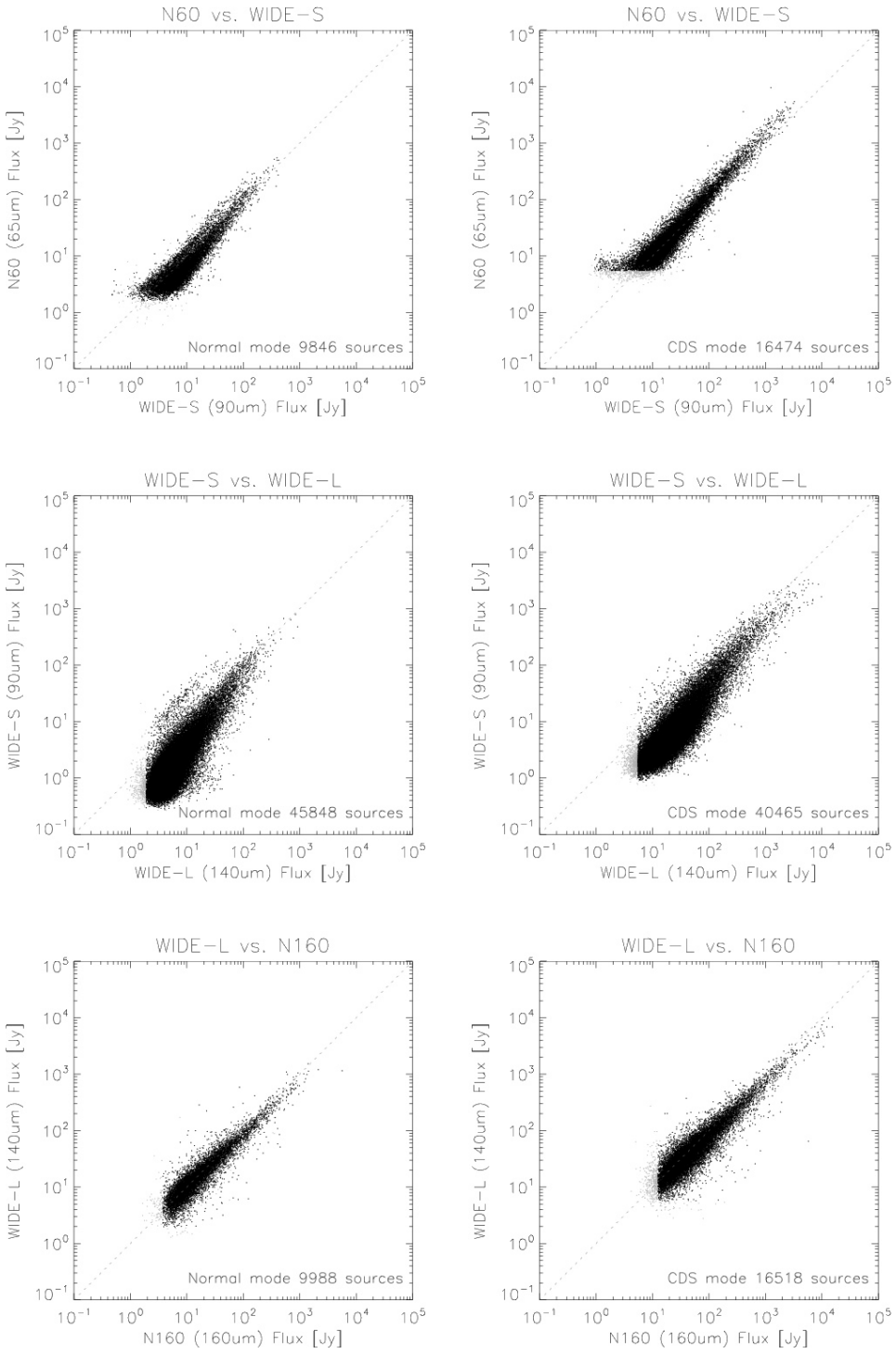

Figure 10: Flux comparison between the AKARI photometric bands. Left panels: *Normal* sampling mode data. Right panels: *CDS* mode data. Black points are $FQUAL = 3$, and Grey points are $FQUAL = 2$.

5.5 Position uncertainty

As described in Section 2.2 the pointing reconstruction processing for the AKARI All-Sky Survey succeeded to provide the position data with an accuracy better than a few arcsec in most of the survey area. However, there are a couple of reasons that degrade the positional accuracy in the catalogue; lower spatial resolution of the FIS instrument, noise and anomalies in data, and influences of sky background structure. In addition, the positions in the current version catalogue are the positions of the peak pixels (on the *logEvidence* map for source extraction) and not actual centroids. The image pixel size is 8 arcsec, so the position information is quantumized to that scale.

The positions in the current AKARI-FIS catalogue is evaluated by comparing with "reference" positions given from external sources. Information from the *Simbad* database is used. Only sources with high accuracy position data are used. Our experiences tell that among the different types of objects those classified as "Emission-line galaxy" give the best results. We have 1658 matches to the object in this category within 20 arcsec.

Figure 11 shows statistics of position disagreement in the Ecliptic longitude and latitude, which are approximately in- and cross-scan direction. The Gaussian fits to the distribution give the standard deviation of 3.8 arcsec in $\Delta\lambda$ ($\sim$ cross-scan) and 4.8 arcsec in $\Delta\beta$ ($\sim$ in-scan) direction, respectively. The values are consistent with the expectation from the fact that our current positions are quantumized in the 8 arcsec pixel grid. Larger error in the in-scan direction is most likely due to transient response of the detectors. We should note that we see systematic 1–2 arcsec offsets of the Gaussian peak position. The offsets are not along a particular coordinates. They do not depend on source positions. In the current version we do not make any correction about these systematic offsets since the cause of this offset is not yet understood, and they are still small compare to the random error.

We do not analyse position error in the *CDS* mode, as it is difficult to find a set of sources with reliable positions in the Galactic plane region where the *CDS* mode was taken. In principle the source extraction process works on this mode as good as the *Normal* mode, but it is possible that bright and complicated background sky influences on the determination of the source position.

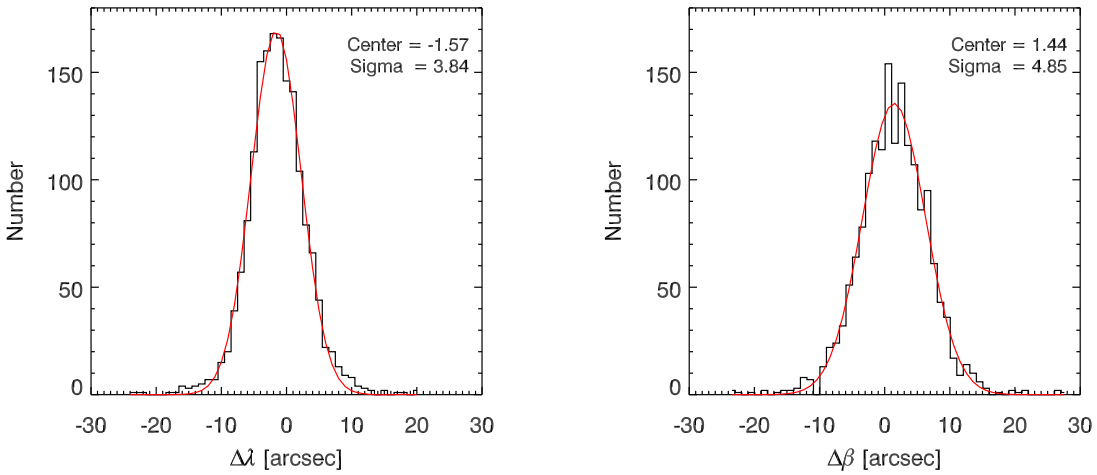

Figure 11: Position disagreement between AKARI-FIS catalogue and those in the *Simbad* database for the objects in the category "Emission-line galaxy". $\Delta\lambda$ ($\cos\beta$ corrected) and $\Delta\beta$ approximately denote cross- and in-scan direction, respectively. All sources locate high Galactic latitude ($|b| \geq 20$ deg) and are observed in the *Normal* sampling mode.

Figure 12 plots the position errors of the sample against their fluxes. To see the trend of data we calculate average values from every 300 sources from the faintest one, and indicate with diamonds. The error-bars show the standard deviation from the average. We see little flux dependency of the position error over the current flux range of the sample. The error of about six arcsec is larger than the sigma presented in Figure 11, since it includes systematic offset in the calculation of the distance. As a practical and safe value, we recommend six arcsec as the current position accuracy for all sources in the catalogue.

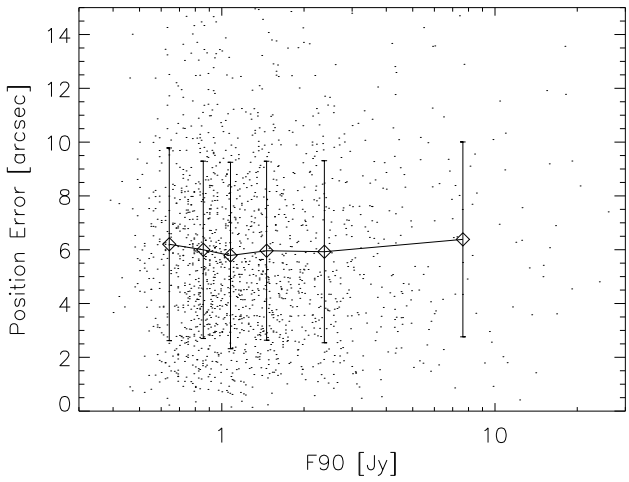

Figure 12: Position disagreement between AKARI-FIS catalogue and those from *Simbad* database for the sources classfied as "Emission-line galaxy" is plotted against their 90 μm flux. Statistics is based on the sources matched within 20 arcsec. Dots indicate individual sources. Diamonds with error-bars are averaged values over every 300 sources (from the faintest one) The error is almost constant around 6 arcsec in this range.

5.5.1 Sky coverage

The AKARI/FIS survey scanned more than 98 per cent of the entire sky during the mission. Figure 13 (*Right*) presents achieved sky coverage in the 90 μm (WIDE-S) band. Only valid observation data are concerened. The area of 98.3 per cent of the entire sky are observed more than twice, 52.0 per cent more than 5 times, and 8.9 per cent by more than 10 scans.

Figure 13 (*Left*) shows a scan density map of the AKARI/FIS survey for the WIDE-S (90 μm) band. In general high visibility is achieved in the high Ecliptic latitude regions. We see small scale variations in the longitude (cross-scan) direction cased by unobserved scan period due to SAA passage, pointed observations, and the Moon light.

Unlike IRAS, however, the unobserved sky regions distribute over the sky as many narrow stripes in the inner Galactic plane. An example is shown in Figure 14. The plot shows the sky distribution of the detected point sources. We see many narrow stripes of without sources. It is not possible to judge only from the catalogue entries whether an undetected object was not observed due to visibility constraint or simply it is too faint. The on-line catalogue access via *AKARI-CAS* will provide the visibility information[3].

[3]The function will be provided later than April 2010

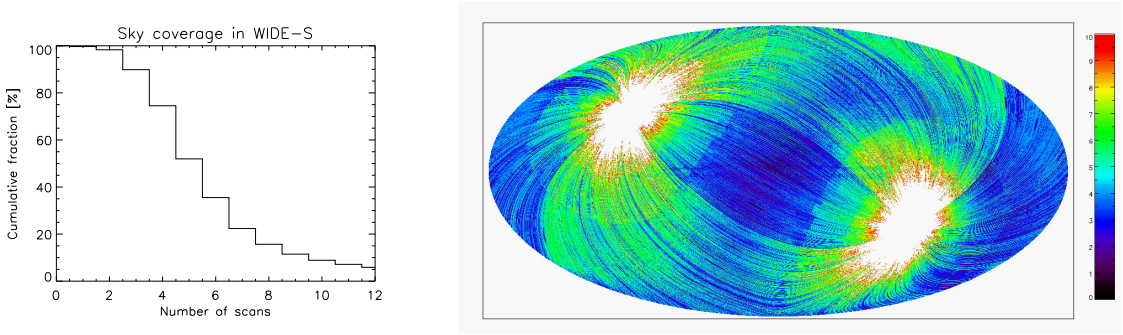

Figure 13: *Left:* The accumulative fraction of sky area observed more than the certain number of scans indicated in the X-axis. *Right:* Scan density map of the AKARI/FIS survey (WIDE-S = 90 μm band) in the Galactic coordinates, corresponding to the source distribution maps shown in Figure 6. The visibility gets higher at high lattitude regions. The scan density is not uniform and shows structures in the scale of the scan width ($\sim$ 10 arcmin).

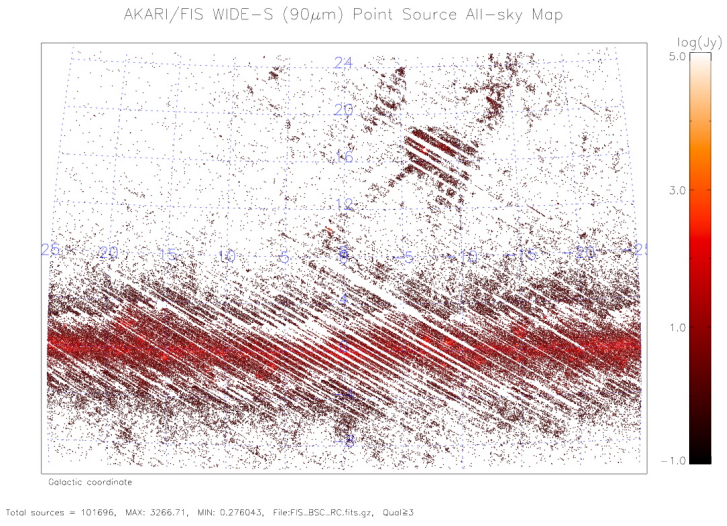

Figure 14: Distribution of detected sources in the inner Galactic plane. We see many narrow stripes of without source. These regions are observed fewer than twice so that source extraction and confirmation were not possible.

6 Comparison with IRAS catalog

6.1 Identification statistics

6.1.1 From AKARI to IRAS

We search for IRAS associations to each AKARI-FIS catalogue source. Scientifically useful AKARI data are those with $FQUAL = 3$. We use all IRAS sources regardless their flux quality flag ($FQUAL$). Matches are taken by position with the search radius of 100 arcsec. If multiple IRAS sources are found for an AKARI source (828 cases) the closest one is taken for the following analysis. A few per cent of AKARI sources have common IRAS counterparts.

The results of the cross-match is presented in Table 8. In general more than 60 per cent of bright AKARI sources have IRAS counterparts. The fraction get worse for the faint sources, and in the crowded regions (for example Galactic plane sampled with the *CDS* mode).

6.1.2 From IRAS to AKARI

In Table 9 we show the statistics of searching AKARI counterparts for IRAS sources. This time we use IRAS sources with $FQUAL = 3$ at 60 or 100 μm bands as an input. The sources located at $|b| \geq 10$ deg are considered. The search is made in the whole AKARI-FIS catalogue, as any of the four bands have $FQUAL$=3. We have quite high ratio of identification for relatively bright IRAS sources. Sources fainter than 1 Jy at 60 μm or 10 Jy at 100 μm result worse statistics, probably due to IRAS detection quality. On the other hand the current catalogue may miss some brightest sources due to detector saturation at WIDE-S band.

6.2 Flux comparison

AKARI and IRAS fluxes are compared for the identified sources in Figure 15. The *Normal* mode and *CDS* modes are indicated in different colour for the consistency check. In these comparisons we only use IRAS sources with best flux quality ($FQUAL = 3$) so the number of identified sources are smaller than those in Table 8. No colour correction is applied. Jeong et al. (2007) compared AKARI and colour corrected IRAS fluxes for the preliminary source list from the data observed during the PV phase.

In general, fluxes given by the two missions are consistent each other with some scatter. Difference in the spatial resolution could cause differences in the 'point source' flux. Current AKARI flux uncertainty is still large (typically 20 per cent). In addition to the scatter we see several noticeable systematic deviation between the data. It is clearer in the plots of flux ratios in Figure 16. We also see strong deviations toward the bright end of N60 and WIDE-S in the *CDS* mode. These anomalies are most likely due to incomplete flux calibration. Further investigation and improvement will be attempted for the future versions.

Table 8: Number of AKARI $FQUAL = 3$ sources and those having IRAS associations.

	Normal mode			*CDS* mode		
Flux range[Jy]	Total	Identified	Rate(%)	Total	Identified	Rate(%)
N60						
< 1	0	0	N/A	0	0	N/A
1 – 10	7483	4546	60.8	3994	955	23.9
10 – 100	3000	2043	68.1	11781	4309	36.6
100 – 1000	310	278	89.7	2000	1295	64.8
$1000 \leq$	6	6	100.0	205	172	83.9
Total	10799	6873	63.6	17980	6731	37.4
WIDE-S						
< 1	176881	30542	17.3	1461	149	10.2
1 – 10	69443	23854	34.4	103301	15879	15.4
10 – 100	4296	2778	64.7	16195	5310	32.8
100 – 1000	184	147	79.9	1684	1151	68.3
$1000 \leq$	0	0	N/A	108	90	83.3
Total	250804	57321	22.9	122749	22579	18.4
WIDE-L						
< 1	0	0	N/A	0	0	N/A
1 – 10	54875	13375	24.4	10122	1579	15.6
10 – 100	10846	4771	44.0	39041	8851	22.7
100 – 1000	547	416	76.1	3598	1861	51.7
$1000 \leq$	8	7	87.5	222	175	78.8
Total	66276	18569	28.0	52983	12466	23.5
N160						
< 1	0	0	N/A	0	0	N/A
1 – 10	6781	2127	31.4	0	0	N/A
10 – 100	7260	3586	49.4	17801	4611	25.9
100 – 1000	662	493	74.5	4031	1944	48.2
$1000 \leq$	19	14	73.7	303	228	75.2
Total	14722	6220	42.2	22135	6783	30.6

Table 9: Number of IRAS sources identified in the AKARI-FIS catalogue. Sources with $FQUAL = 3$ at IRAS 60 μm and 100 μm bands in $|b| > 10$ deg are searched in the AKARI $FQUAL = 3$ (at any band) samples.

	IRAS 60 μm ($FQUAL = 3$)			IRAS 100 μm ($FQUAL = 3$)		
Flux range[Jy]	Total	Identified	Rate(%)	Total	Identified	Rate(%)
< 1	18890	12600	66.7	1315	225	17.1
$1 - 10$	9176	8429	91.9	33743	13544	40.1
$10 - 100$	592	585	98.5	1278	1163	91.0
$100 - 1000$	56	51	91.1	62	60	96.8
$1000 \leq$	7	5	71.4	11	6	54.5
Total	28723	21670	75.4	36409	14998	41.2

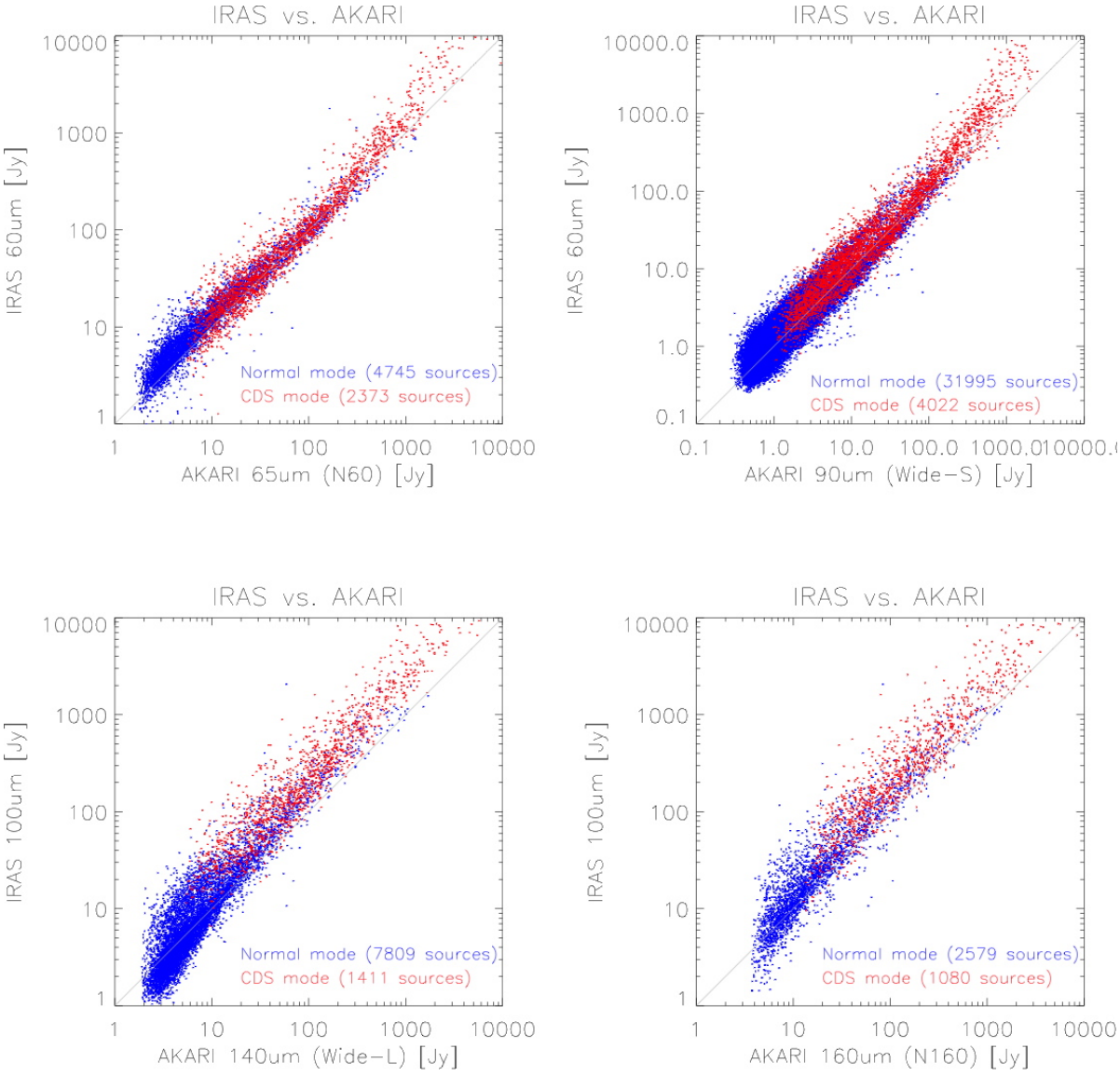

Figure 15: Comparison of AKARI and IRAS fluxes. AKARI data are only those of $FQUAL = 3$. No colour correction has been applied.

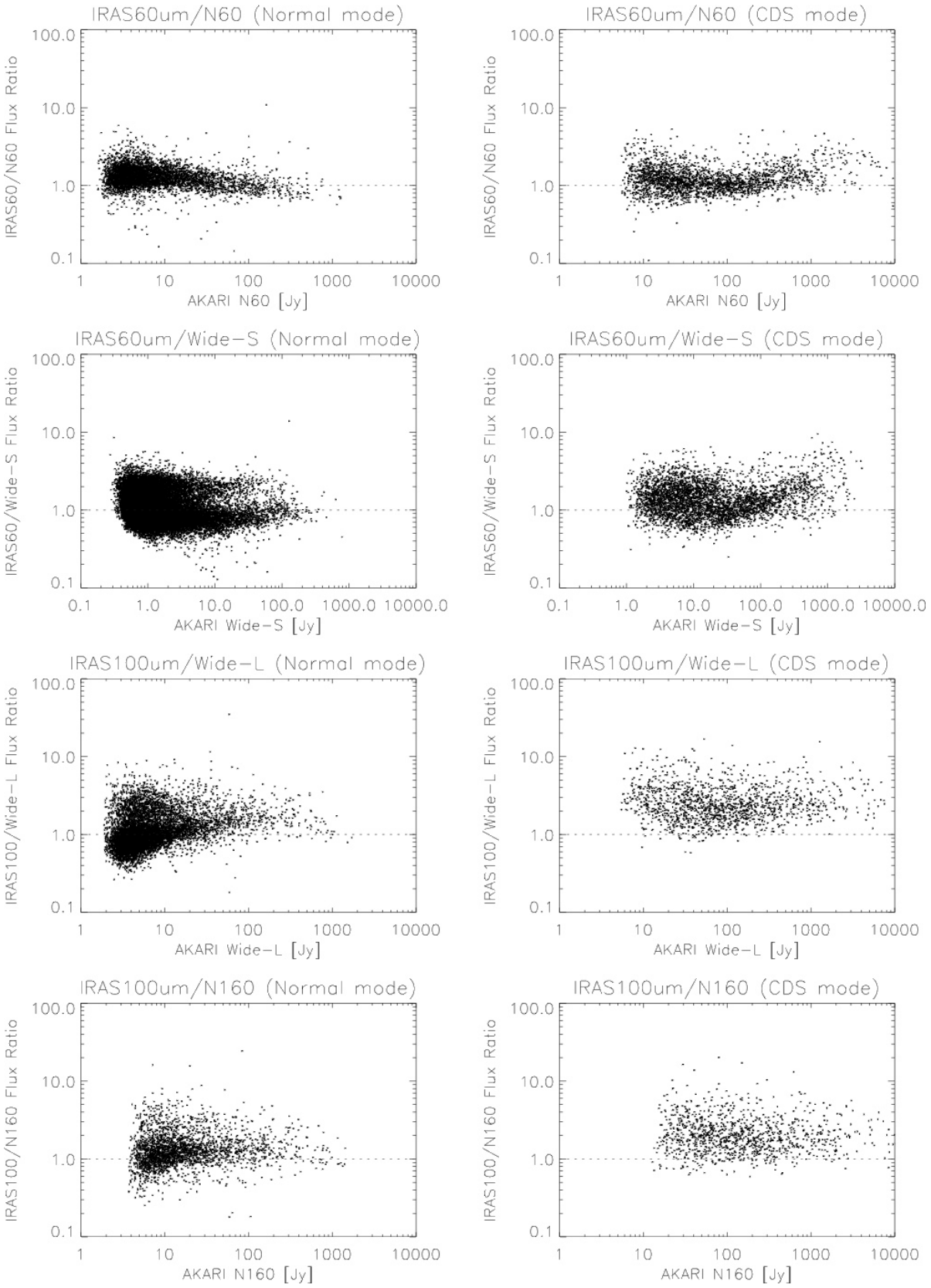

Figure 16: Flux ratios of AKARI and IRAS bands. The *Normal* and *CDS* mode data are plotted separately. AKARI data are only those of $FQUAL = 3$. No colour correction is applied so the ratios do not have to be 1.0.

6.3 Comparison with other FIR photometry

The AKARI-FIS catalogue fluxes are compared with two other far-infrared photometries.

Table 10 compares the fluxes of the current catalogue with those by the AKARI/FIS Slow-scan observations. The data are taken from Table 7 of Shirahata et al. (2009,) in which flux calibration of the Slow-scan mode is described. Both stars and infrared luminous galaxies, from 0.6 Jy to 100 Jy, are included in the sample. Number of commonly observed sources and weighted average of the flux ratios ($F_{\rm BSC}/F_{\rm Slow-scan}$) are presented. Weight is taken from the flux uncertainty in the catalogue. The two observing modes provides consistent flux values within 10 per cent. We do not see any significant differences between the stellar sample and galaxy sample in WIDE-S that measured sufficient numbers of both kinds of objects.

Table 10: Comparison of flux in the BSC with that in Shirahata et al. (2009).

Band	Number of sources	Average flux ratio[1]
N60	10	1.05
WIDE-S	21	0.99
WIDE-L	5	1.02
N160	2	0.92

[1] $F_{\rm BSC}/F_{\rm Slow-scan}$.

Table 11 presents comparison between the AKARI/FIS and the ISO/PHOT measurements. The sources are all UIRLGs reported by Klaas et al. (2001). They observed 41 object in 10 wavelengths, including those in the far-infrared range at 60, 90, 120, 150, 180, and 200 μm. The fluxes in the 90 μm band are between 0.6 and 100 Jy. We compare ISOPHOT 60 μm fluxes directly with FIS/N60 (65 μm) measurements. For WIDE-L (140 μm) and N160 (160 μm), we estimate the flux at the FIS wavelengths by interpolating the fluxes at the adjacent ISO bands.

Table 11: Comparison of AKARI/FIS fluxes with those in Klaas et al. (2001).

Band	Numbe of sources	Average flux ratio[1]
N60 / PHOT 60 μm	27	0.84
WIDE-S / PHOT 90 μm	34	0.91
WIDE-L / (est)[2] 140 μm	28	0.99
N160 / (est)[2] 160 μm	8	1.14

[1] $F_{\rm BSC}/F_{\rm Slow-scan}$.
[2] Estimated by interpolating the fluxes at the adjacent bands.

Relatively large difference in the N60 / ISOPHOT 60 μm band is due to the difference in the wavelength (65 vs. 60 μm). The other bands are well consistent to each other.

7 Remarks on the FIS Bright Source Catalogue

7.1 Source Name

As we write in the earlier sections, the sources in this catalogue must be referred to in the literature such as AKARI-FIS-V1 J0123456+765432.

7.2 Use $FQUAL = 3$ sources

Use only sources with $FQUAL = 3$ for secure scientific analysis. Sources with $FQUAL = 2$ or 1 may have flux values, but they are not always reliable.

7.3 Moving sources and Months confirmation

Most of the moving sources, Solar-System objects or space debris should be filtered out by the Hours confirmation process (Section 2.4). The Months confirmation flags (*MCONF*) further assure the object being really celestial. Because of the visibility constraint of the AKARI Survey, some sky regions were observed only by scans within a month (usually in a few days). $MCONF = 0$ does not always mean that the source is unreliable.

7.4 *CDS* calibration

The fluxes of very bright sources ($>$ a few undred Jy) in the *CDS* mode may be underestimated especially in N60 and WIDE-S bands (Figure 15, 16).

7.5 Very bright sources

It has been known that very bright ($\geq$ 100 Jy) sources may have unreliable fluxes or even undetected. A reason is detector saturation. Also it is possible that peaks of such bright signals are mis-identified as glitches and flagged out. We plan to solve this in the future versions.

7.6 Low-flux sources

There are Hours confirmed sources with very low flux compared to the detection limits. The possible reason of this is discussed in Section 5.1. These fluxes are not reliable, and should be avoided for the scientific discussions. Sources with flux lower than 1/2 of the detection limits are distinguished by the 2nd bit (bit 1) of *FLAGS* of the corresponding band. If the source has $FQUAL65 = 3$ (Hours confirmed), it is degraded to $FQUAL65 = 2$. Numbers of $FQUAL = 2$ sources are summarized in Table 12.

Table 12: Number of sources with too low flux.

Band	Total	*Normal* mode	*CDS* mode
N60	570	64	506
WIDE-S	1471	301	1170
WIDE-L	4270	2205	2065
N160	1781	814	967

7.7 False detections due to "Side-lobe" effect

The *logEvidence* map on which source detection is performed exhibits a ring-like feature around bright sources. We understand that this is caused by the extended components in the real PSF emphasized in the calculation of the *logEvidence* map. As a result false detections may be included in the catalogue.

We have developed a set of mask to flag out such false sources. The left panel in Figure 17 shows source number density around $\sim 14,000$ brightest sources in WIDE-S by white contours overlapped on a *logEvidence* map around a $F_{90} = 290$ Jy source. There is a clear coincidence between the contours and the colour image. We found little dependency of the pattern to the sky position. The red line indicates the masked areas. On the right panel of the figure relative intensities of sources on the side-lobe to the main object are plotted. The thick line presents the upper limit. We apply combination of two conditions, position and relative intensity, to distinguish the false sources. Total 10,227 sources are flagged.

The possibility that the real sources are flagged by chance is estimate to be 8–9 per cent (of the flagged sources) by applying the masks from the real sources to randomly selected different sky regions.

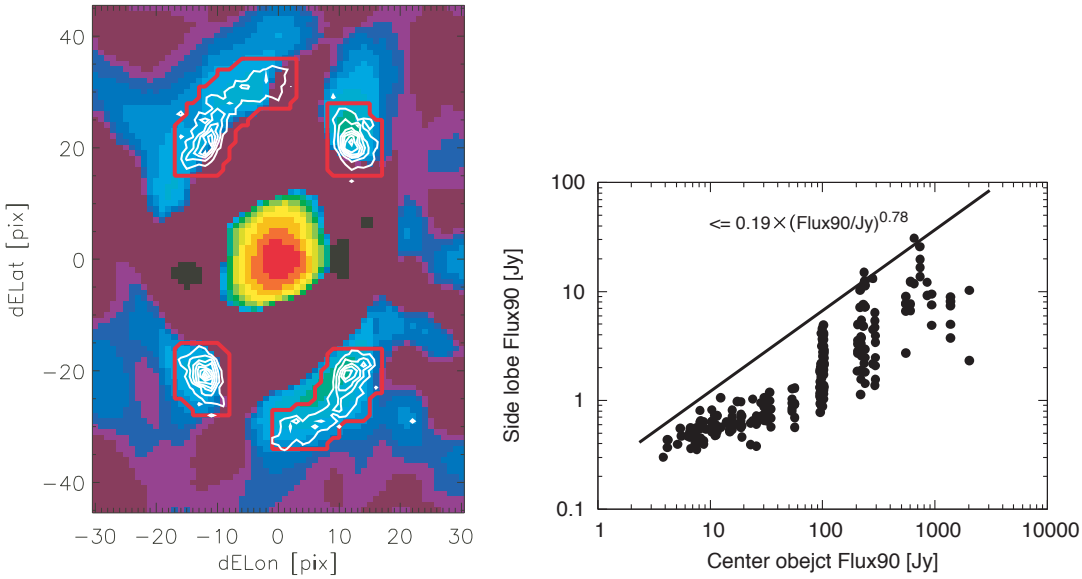

Figure 17: *Left:* The number density of sources around a bright source is plotted in white contours on top of a *logEvidence* map around a $F_{90} = 290$ Jy source (colour image). The image pixel size is 8 arcsec. We see clear concentration of sources at the high *logEvidence* positions. *Right:* Relative intensity of the sources on the side-lobe to the main source. The thick line indicates the upper-limit. Combination of two conditions can detect the false detections efficiently.

Acknowlegements

AKARI is a JAXA project with the participation of European Space Agency (ESA). Development of the satellite and instruments, operation, and data reduction have been carried out under the collaborations with the following institutes; Nagoya University, The University of Tokyo, National Astronomical Observatory Japan. The far-infrared detectors were developed under collaboration with The National Institute of Information and Communications Technology. The Seoul National University (Korea), and a consortium including Imperial College University of London, Open University, University of Kent, Sussex University, and SRON-Groningen with University of Groningen has participated in the data reduction of the All-Sky Survey. UK work has been supported by The Particle Physics & Astronomy Research Council, The Science and Technology Facilities Council, The Daiwa Anglo-Japanese Foundation, The Royal Society and The Great Britain Sasakawa Foundation, to whom we are extremely grateful.

We use the SIMBAD database, operated at CDS, Strasbourg, France.

REFERENCES

Cohen, M., Walker, R. G., Carter, B., Hammersley, P., Kidger, M., Noguchi, K., 1999, AJ, 117, 1864
Cohen, M., Megeath, S. T., Hammersley, P. L., Martin-Luis, F., Stauffer, J., 2003, AJ, 125, 2645
Cohen, M., Wheaton, W. A., Megeath, S. T., 2003, AJ, 126, 1090
IAU Recommendations for Nomenclature, Version 2006 November 28, *http://cdsweb.u-strasbg.fr/iau-spec.html*
Jeong, W.S., et al., 2007, PASJ, 59, S429
Kataza, H., et al., 2009, "AKARI/IRC All-Sky Survey Bright Source Catalogue Version *beta*-1 – Release Note (Rev.1) –"
Kawada, M., et al., 2007, PASJ, 59, S389
Klaas, U., et al., 2001, A&A, 379, 823
Moreno, R., 2007, private communication
Müller, T. G., & Legerros, J. S. V., 1998, A&A, 338, 340
Müller, T. G., & Legerros, J. S. V., 2002, A&A, 331, 324
Murakami, H., et al., 2007, PASJ, 59, S369
Onaka, T., et al., 2007, PASJ, 59, S401
Savage, R. S., Oliver, S., 2007, ApJ, 661, 1339
Shirahata, M., et al., 2009, PASJ, 61, 737
Verdugo, E., Yamamura, I., Pearson, C. P., 2007, "AKARI FIS Data Users Manual ver. 1.3"